# Tantalum Oxynitride Nanotube Film Arrays for Unconventional Nanostructured Photo-electrodes Active with Visible Light

Francesco Tavella[a b], Chiara Genovese[a], Felipe Andrés Garcés Pineda[b], Gabriele Centi[a], Siglinda Perathoner[a], Claudio Ampellia

[a] *Department of Chemical, Biological, Pharmaceutical and Environmental Sciences (ChiBioFarAm), University of Messina, ERIC a.i.s.b.l. and CASPE/INSTM, Viale Ferdinando Stagno d'Alcontres, 31, 98166 Messina, Italy*

[b] *Institute of Chemical Research of Catalonia (ICIQ), The Barcelona Institute of Science and Technology (BIST), Av. Paisos Catalans 16, 43007 Tarragona, Spain*

## Abstract:

Tantalum-oxy-nitride nano-ordered nanotubes ($TaO_xN_y$ NTs) for film-type electrodes were successfully synthesised through anodic oxidation of metallic Ta followed by high-temperature annealing in an $NH_3$ atmosphere to prepare unconventional nanostructured photoactive electrodes active with visible light. Their morphology was studied by scanning electron microscopy (SEM-EDX), showing that the tube length and inner diameter correlate with the synthesis parameters. The nitridation temperature was also investigated, showing that the conversion of bare $Ta_2O_5$ into TaOxNy strongly influences the absorption in the visible region with a bandgap shift from 4.0eV of the $Ta_2O5$ NTs to 2.1eV of the $TaO_xN_y$ NTs treated at 800°C. Photo-electrochemical and catalytic performances were evaluated with chronoamperometric measurements and different photo-reaction using AM 1.5 G solar simulator light: (i) degradation of methylene blue (MB), (ii) ethanol gas-phase photo-reforming and (iii) bias-assisted photoelectrochemical water splitting. The nitridation temperature increases the degree of N- substitution in $TaO_xN_y$ NTs, increasing the visible light photocatalytic performances. The $TaO_xN_y$ NTs film-type electrode, obtained by nitriding at 800°C, shows the highest photocurrent value (0.1 mA·cm$^{-2}$), MB's highest rate of degradation, and $H_2$ photo-production.

## Keywords

Tantalum Oxynitride, TaON nanotube array, nanostructured film electrodes, ethanol photoreforming, $H_2$ photocatalytic production, visible-light photocatalysis

## Introduction

The interest in visible-light photoactive materials is drastically increasing for applications going from environmental remediation [1, 2] to $H_2$ photocatalytic production or $CO_2$ reduction [3-6] as part of the general effort towards renewable-energy-driven processes [7-11]. Photocatalytic water splitting, in particular, has largely attracted research interest. An intense effort was dedicated to developing semiconductor materials with a band-band within the visible range since the discovery of Honda and Fujishima of the photocatalytic properties of $TiO_2$ in the late 1970s [12]. While the application has now been scale-up to a large (100 $m^2$) demonstration unit using modified, aluminium-doped strontium titanate particulate photocatalysts [13], the solar-to-hydrogen (STH) efficiency is still low (STH=0.76%), and downstream separation of $H_2$ and $O_2$ is required.

A photoelectrocatalytic (PEC) approach, where the production of $H_2$ and $O_2$ occurs in physically separated compartments, is preferable from this perspective [14]. Avoiding liquid electrolytes, with the membrane acting as both the element separating the anodic/cathodic sections and closing the ionic transport circuit, is also a preferable engineering choice because it reduces costs and improves scalability [15, 16]. However, this reactor design requires that the photoanode has a specific configuration allowing high light harvesting and efficient collection of the photogenerated current together with the transport of the photogenerated protons from water photo-oxidation to the membrane located on the back of the photo-anode [17, 18]. An ordered array of vertically-aligned semiconductor nanotubes (NTs) grown over a perforated metallic foil (acting as an electron collector) would be ideal for achieving these objectives [19-21].

As cited above, we used this nanostructured film electrode (based on $TiO_2$ NTs film array) in PEC applications for water splitting and $CO_2$ reduction. Preparing these materials by controlled anodic oxidation of Ti foils is an established technology [22-25]. We also have studied several aspects of their synthesis and use in various photoactive reactions [26-29]. $TiO_2$ is attractive as a semiconductor for various reasons: stability, eco-compatibility, corrosion resistance, good absorption of ultraviolet light, etc. Still, the main limit is the activity only with ultraviolet light, e.g., about 4% of the incident solar light. Many studies have been made to improve visible-light activity by doping, heterojunctions, plasmonic effects, etc. Still, progress has been limited, and in several cases, the methods are not well suited to modify the properties of $TiO_2$ NTs film-type electrodes [30-33].

The conversion of oxides to oxynitrides is a well-established method for particulate photocatalysts to shift the band gap within the visible region [34-36]. Among oxynitrides, Tantalum OxyNitride ($TaO_xN_y$) show interesting performances [37-40]. Semiconductors such as TaON [41] and $Ta_3N_5$ [42, 43] possess an interesting band structure,, in the ~2.2-2.7 eV range depending on the amount of N

present in the structure, allowing a theoretical solar-to-hydrogen efficiency as high as 15.9% under AM 1.5 G 100 mW·cm$^{-2}$ irradiation [43].

TaO$_x$N$_y$ compounds can be obtained through high-temperature treatment in an NH$_3$ atmosphere of Ta$_2$O$_5$. However, most of the studies regarding particulate materials, while limited studies reported the synthesis and use of nanostructured film-type electrodes characterised by an ordered array of vertically-aligned NTs [24, 38, 42, 44] and on the preparation by anodic oxidation of the ordered array of Ta$_2$O$_5$ NTs [45-50].

Starting from our previous experience with nanostructured TiO$_2$, we synthesise Ta$_2$O$_5$ nanotubes through anodic oxidation of metallic Ta. Anodic oxidation of metals is a technique that allows easily obtaining the desired morphology of the resulting oxide by simply changing the right synthesis parameters [51-53]. For example, extending the anodisation time usually increases the oxide film thickness while the composition of the electrolyte consent to grow the oxide layer in different shapes (tubes, rods, honeycombs, etc.) [54-56]. This work analyses the correlation between synthesis parameters, the resulting morphology and the photocatalytic performances of electrodes based on TaO$_x$N$_y$ NTs ordered array. The photocatalytic activity of the tantalum TaO$_x$N$_y$ NTs varying the synthesis parameters and the nitridation temperature was also investigated.

## Material and methods

### Preparation

***Synthesis of Ta$_2$O$_5$ NTs film array.*** A two-step anodisation process was made. First, Ta discs (35 mm diameter, 0.125 mm thickness, supplied by Alfa Aesar) were pre-treated with 400 and 600-grit abrasive paper and later sonicated in isopropyl alcohol for 30 min. Two different electrochemical baths were used. The first consisted of ethylene glycol with 0.33%wt of NH$_4$F and 3%vol of H$_2$O. The second electrolyte was composed of H$_2$SO$_4$ (98% Sigma Aldrich) with HF 1%vol (30% Sigma Aldrich) and 4%vol H$_2$O. Agilent E3612A DC Power Supply and Keithley 2000 multimeter were used to apply the desired voltage and measure the current during anodisation. Applied potential ranged from 20 to 60V, and time varied from 1min to 1h. After the anodisation, the samples were sonicated in H$_2$O to remove the oxide, and the resulting Ta foil was used for a second anodisation step.

***Conversion to TaO$_x$N$_y$.*** The Ta$_2$O$_5$ NTs film array samples were annealed in a quartz tubular furnace under a flow of 20mL min$^{-1}$ of NH$_3$ (10%He) to convert the tantalum oxide nanotubes to TaO$_x$N$_y$. The temperature ranged from 600 to 900°C at a heating rate of 25°C min$^{-1}$ and then kept constant for the entire treatment time of 3h. The samples reported as oxide were annealed in a muffle furnace at 450°C for 3h.

### Characterisation

UV-visible Diffuse Reflectance Spectroscopy measurements were performed by a Thermo Fischer 220 Spectroradiometer equipped with an integrating sphere for solid samples, using $BaSO_4$ as the reference and in the air. Scanning Electron Microscopy (Phenom ProX Desktop) was used for structural and morphological characterisation operated at an accelerating voltage of 10 kV. The nanotube diameter and length were directly measured from SEM images. Photoelectrochemical measurements were performed in a three-electrode cell equipped with a quartz window. A Pt wire was used as the counter electrode, and a 3M KCl-Ag/AgCl as the reference electrode. All measurements were performed at room temperature in 1 M $Na_2SO_3$ solution at 0.3 V using a 2049 AMEL potentiostat-galvanostat.

**Photocatalytic tests**

Three different types of testing were conducted. The degradation of methylene blue (MB) was carried out in a home-made glass flask equipped whit a quartz window that allows the catalysts to be irradiated: the samples were suspended inside the reactor, 150 mL of 10μM MB aqueous solution was stirred in the dark for 30 min under nitrogen flow (10 mL min$^{-1}$) at room temperature. Samples were taken out at regular intervals, and MB concentration changes were monitored using UV/Vis at a wavelength of 665 nm. The second type of test was made using the same flask equipment discussed above, but in gas phase configuration, essentially 20 mL of EtOH was placed on the bottom of the flask and heated at 60°C under slow stirring. The catalysts were suspended inside the reactor, and samples were taken out at regular intervals and sent to GC (Agilent 7890A) for product detection. The third test was conducted in an H-type electrochemical cell with a quartz window. The anode was the Ta-based material, and the cathode was a platinum tip. Ag/Ag-Cl was used as a reference electrode. The electrolytes used were $Na_2O_3$ 0.1 M in the anode chamber and $H_2SO_4$ 0.5 M in the cathode chamber. The two electrolyte compartments were separated with a reinforced fluorinated Nafion membrane. Products were detected using Hiden analytical HPR-20 R&D mass spectrometer. For all the experiments discussed, the light source was a Xe-arc lamp (ORIEL, 300W) with the addition of an AM 1.5G solar simulator filter.

**Results**

**Synthesis of the photoelectrode and their characteristics**

***Factors controlling the features of the Ta$_2$O$_5$ NTs film array***. Based on previous experience synthesising Ti nanotubes [54], we initially used an ethylene-glycol-based electrolyte. Figure 1a reports an SEM (scanning electron microscopy) image of Ta oxide prepared by one step of anodisation in ethylene glycol with NH$_4$F as a fluorine source and 4% vol. of H$_2$O. Figure 1b shows an SEM image of a sample prepared with HF as a direct fluorine source. In both images, an irregular porous oxide structure (with pores ranging from 40 to 100 nm) can be observed. There is no evidence of a tubular structure. However, the sample prepared with HF shows a more homogeneous surface. These first

results prove that the methodologies optimised for preparing a well-homogeneous film array of vertically-aligned TiO$_2$ NTs cannot be applied directly to the tantalum-oxide case.
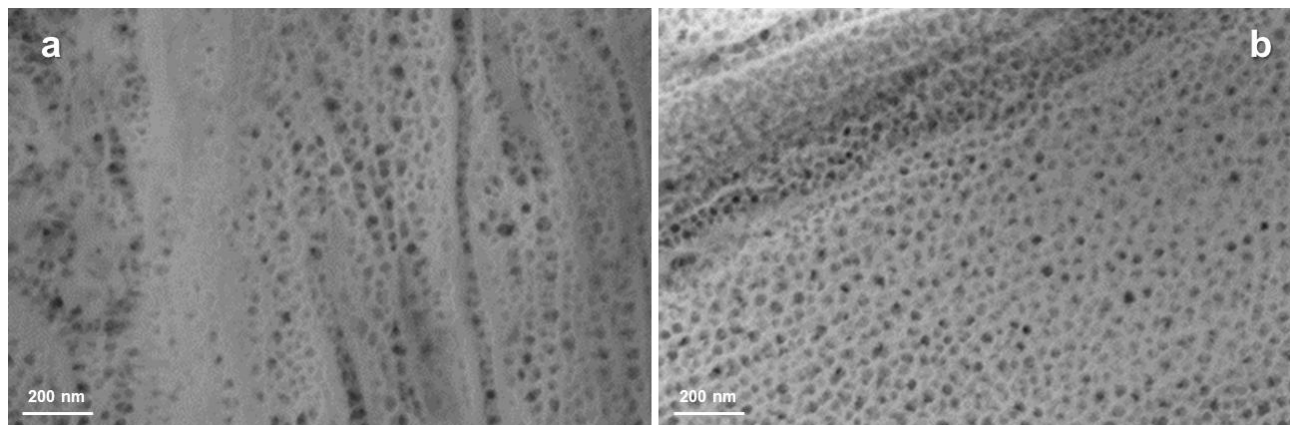


**Figure 1**. SEM images of Ta oxide anodised in EG-based electrolyte: a) with NH$_4$F as fluorine source and b) with HF as fluorine source.

To improve the preparation, we thus moved to the use of H$_2$SO$_4$ as the main electrolyte, in agreement with literature indications [57]. Figure 2 shows the SEM images of the sample prepared at 60 V for 10 min using this electrolyte. The sample was rather inhomogeneous. Ta oxide nanopores did not completely cover their surface. The cross-section image (Figure 2a) confirms the presence of a nano-tubular structure but without the highly ordered array structure, which is the major responsibility for the increase in the catalytic activity of these materials. Particularly, the presence of nano-islands with flower-like tube organisation can be observed in Figure 2b.
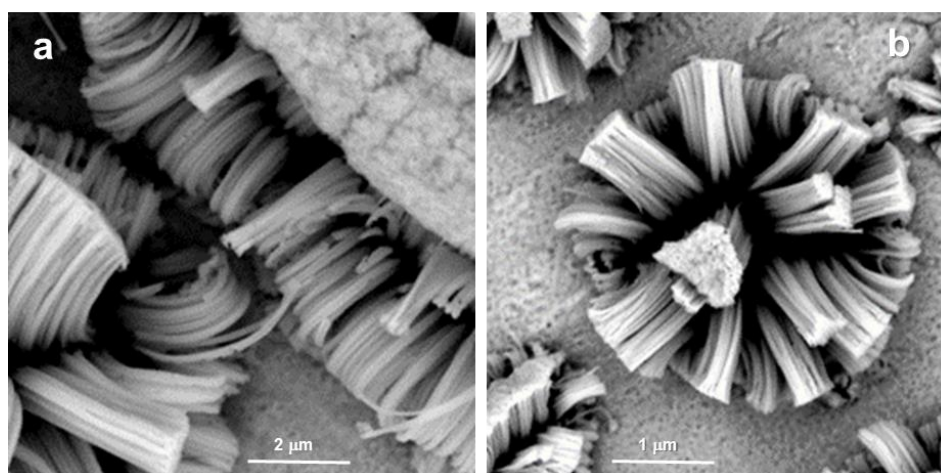


**Figure 2**. SEM image of Ta$_2$O$_5$ nanotubes, a) cross-section image, b) flower-type island nanotubes.

A double step of anodisation was performed to obtain a more robust and homogeneous photoactive layer. After the first anodisation step, the nanostructured oxide layer was rinsed with deionised water and then removed by ultrasonic treatment for 30 min in water. The remaining Ta substrate was then

anodised in a second anodisation step. The diagram in Figure 3 depicts the Ta/Ta$_2$O$_5$ nanostructured electrode. SEM images show the different steps of the nanotube formation.

Specifically, Figure 3a shows the top view of the Ta$_2$O$_5$ NTs film array, evidencing a homogeneous structure with a honeycomb aspect. Figure 3b shows the resulting oxide layer after the membrane detachment, revealing the template used for the second anodisation step. Figure 3c shows the upside-down view of the nanotube oxide membrane, indicating that the bottom of the tubes is closed. Figure 3d shows the cross-section image of the membrane, revealing the high 1-D nano-order needed for improving the charge transport to the metallic collector layer, the remaining not anodised tantalum.
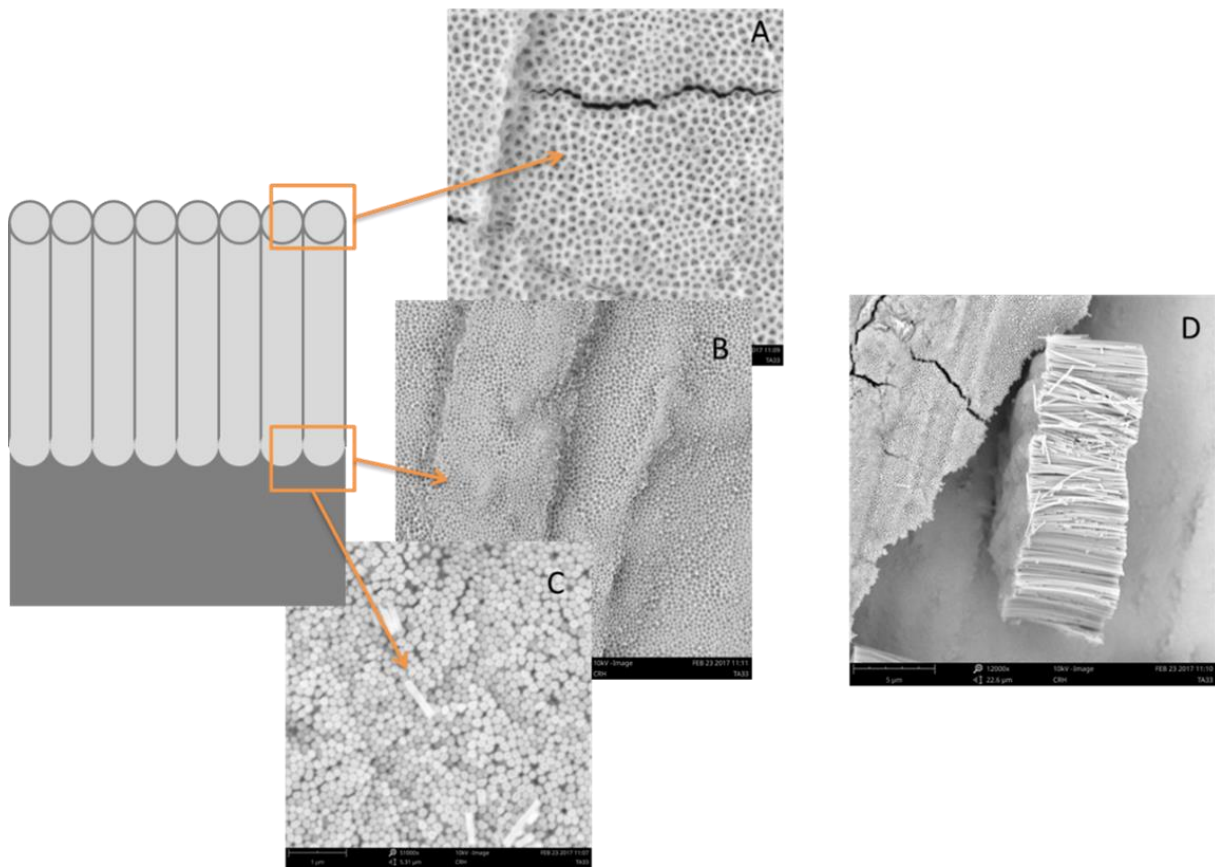


**Figure 3**. Schematic representation and SEM images of the different Ta/Ta$_2$O$_5$ NTs film array layers. SEM images: a) top view, b) reaming template after sonication, c) upside down view of the membrane, and d) cross-section image.

Figure 4 shows the SEM images of the Ta$_2$O$_5$ NTs film array obtained by the double-step anodisation technique at 40 V (10 min for each step). The NTs film array appears quite compact and homogenous. The pores at the top surface are the opening of the nanotubes, while no interstitial spaces are present among the nanotubes.
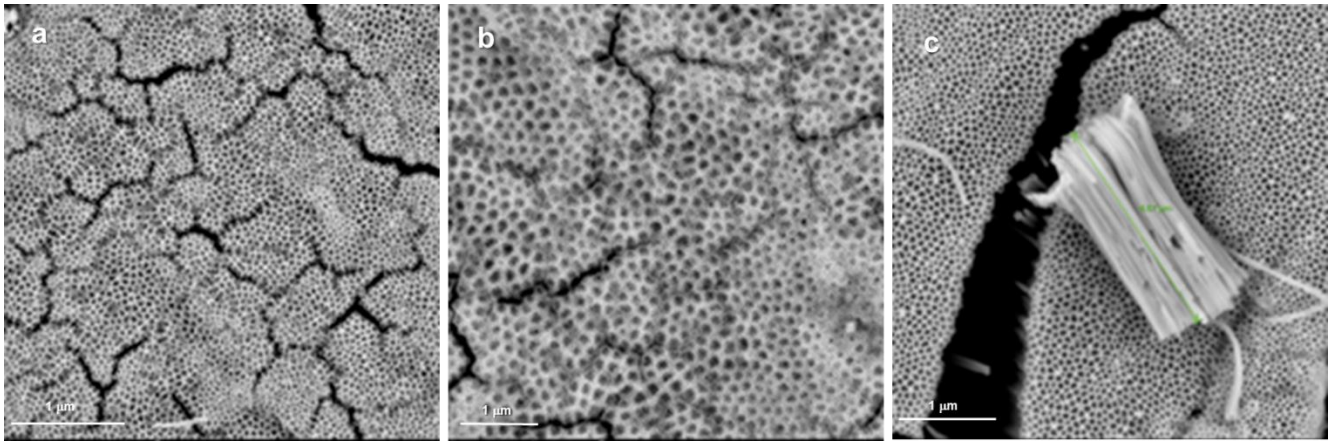
**Figure 4**. SEM images of a) low magnification of $Ta_2O_5$ nanotubes, b) high magnification, and c) cross section obtained from a detached piece of nanostructured Ta oxide.
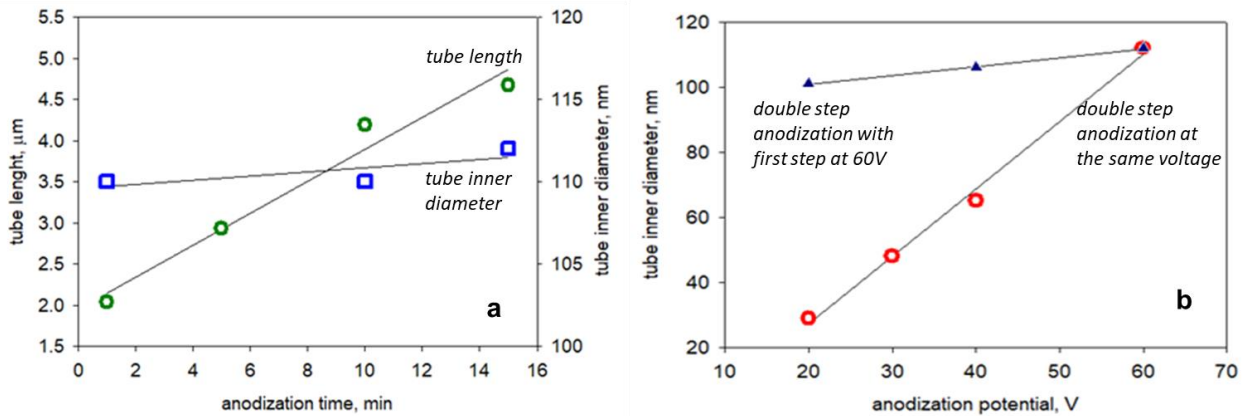


**Figure 5**. Relationship between voltage and time on tube morphology for a) single-step anodisation and b) double-step anodisation. Symbols are the experimental data, while the lines indicate the linear fitting by regression.

The effect of the anodisation time and applied potential was investigated in detail. Figure 5a shows the relationship between time and tube length. We obtained tubes of about ~2μm length in around one min of anodisation and up to ~5 μm in 15 min of anodisation. A faster process is present than Ti anodisation to form $TiO_2$ NTs [54, 58, 59]. Figure 5b shows the profile of the inner diameter of the tubes versus the applied potential. The red circle shows the samples that were anodised at the same voltage in both anodisation steps, while the blue triangle shows the samples that were anodised in the first step at 60V. Results demonstrate that the first step of anodisation mainly controls the inner diameter of the nanotubes. The sample anodised at 60V/20V possesses an inner diameter much wider than the sample anodised at 20V/20V.

*Nitridation procedure*. The nitridation of $Ta_2O_5$ NTs to $TaO_xN_y$ NTs was made by annealing in the 500-800°C temperature range under ammonia flow for different times (from 2 to 6 h). This high-

temperature post-treatment was needed to partially replace the O atoms with N in the $Ta_2O_5$ lattice. This treatment shifts the high bang gap of $Ta_2O_5$ (4.2 eV) to a lower value (~2.1eV). The decrease of the band gap is proportional to the N loading. However, $TaO_xN_y$ NTs films show mechanical issues, as they did not have strong adhesion to the underlying Ta substrate and suffer from serious cracking and peeling-off of the nanotubes from the substrate.
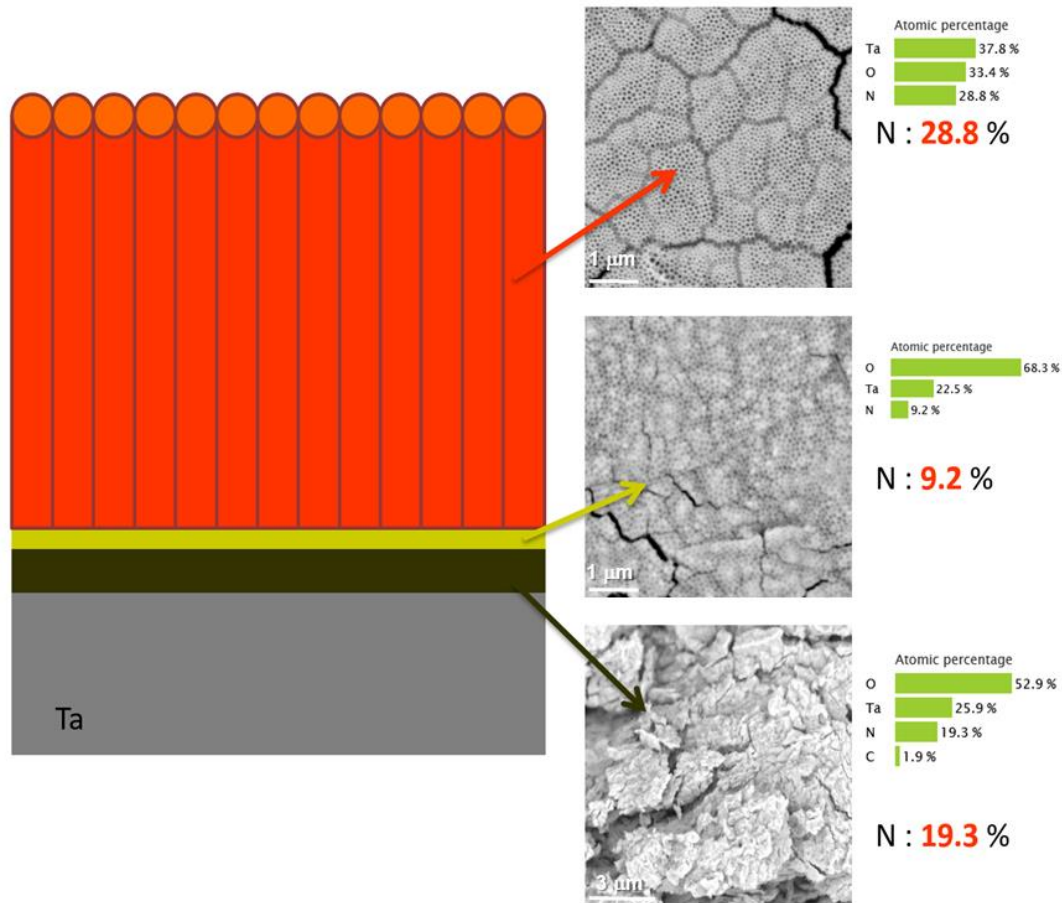


**Figure 6**. Schematic illustration of different layers of $TaO_xN_y$ NTs electrodes after the nitridation process, EDX data reported for sample nitrided at 900°C for 3h.

Figure 6 schematically describes this effect as a function of the nitridation degree with the support of SEM images and EDX analysis. These are samples obtained by the two-step anodisation procedure. The $TaO_xN_y$ NTs, show a highly ordered tubular architecture (the orange part in the picture), with about 28% of nitrogen (as shown by EDX analysis). Under the nanotubes, a further oxide layer can be observed (the yellow layer in the picture), having a reduced replacement of oxygen with nitrogen, about 9%. Furthermore, another Ta oxide amorphous layer was detected (reported in black in the picture) over the metallic Ta remaining non-oxidised. The nitrogen concentration in this layer is about

19%. This amorphous layer is likely responsible for the poor adhesion of the $TaO_xN_x$ NTs film array to the metallic Ta substrate.

EDX results, reported in Figure 7, show that by increasing the nitridation temperature, the quantity of N increased: from 2.7% at 500°C to 19.1% at 900°C. EDX analysis also shows the presence of S in the sample nitride at 500°C, probably coming from the electrolyte bath and not present at higher temperatures.
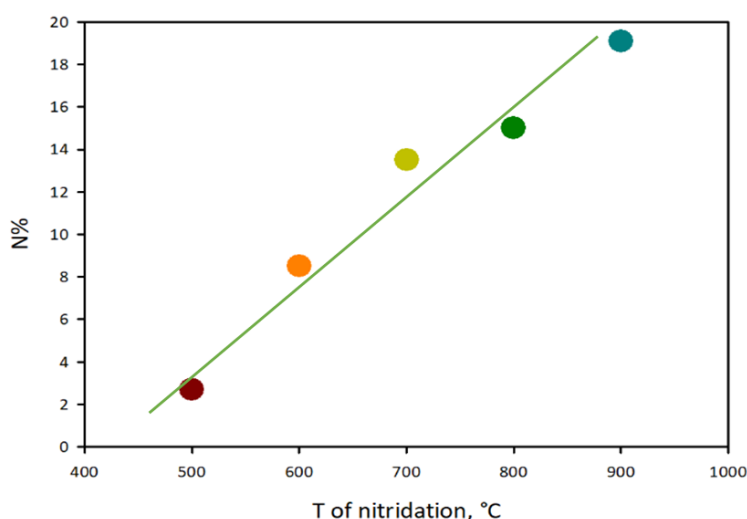


**Figure 7**. EDX atomic percentages wt. of nitrogen (N%) in $TaO_xN_y$ NTs film array samples as a function of the nitridation temperature (T).

***Light absorbance characteristics***. The UV-visible spectra of the $TaO_xN_x$ NTs film array annealed in $NH_3$ at different temperatures are reported in Figure 8. In all the spectra, the characteristic high absorbance in the UV region of the bare Ta oxide can be observed. However, $TaO_xN_x$ NTs show a wide absorption in the visible region due to the modification of the band gap and spe4cially the defects in the oxide, leading to lower energy defect states [35, 37].

The temperature increase in the nitridation steps leads to a well-defined peak at 540 nm for the sample nitride at 700°C and 550nm for the sample nitride at 800°C. At higher nitridation temperatures (900°C), however, the $TaO_xN_x$ NT shows very poor mechanical stability and is thus omitted from Figure 8.

The band gaps (BGs) were estimated from the data in Figure 8 by using the Tauc-plot method. Figure 9 reports the BG calculation for the $Ta_2O_5$ commercial powder showing a BG of 4.0 eV. For the $Ta_2O_5$ NTs (annealed at 500°C in the air), a shift to 3.9eV is observed, consistent with observations for $TiO_2$ powder and $TiO_2$ NTs. The sample nitrided at 800°C shows a BG of 2.01eV, demonstrating that the nitridation procedure converts $Ta_2O_5$ to $TaO_xN_x$. For the samples prepared at 500°C and 600°C

the estimation of the BG is not precise due to the presence of too many defects, creating a large diffuse absorption in the visible region [58].
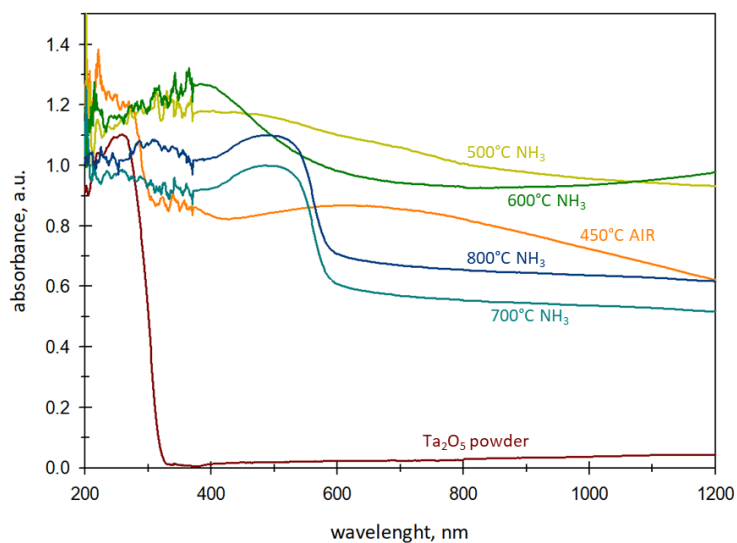


**Figure 8**. UV-visible spectra of $TaO_xN_x$ NTs film array treated at different nitridation temperatures. $Ta_2O_5$ nanotubes (450°C AIR) and commercial $Ta_2O_5$ powder are reported as references.
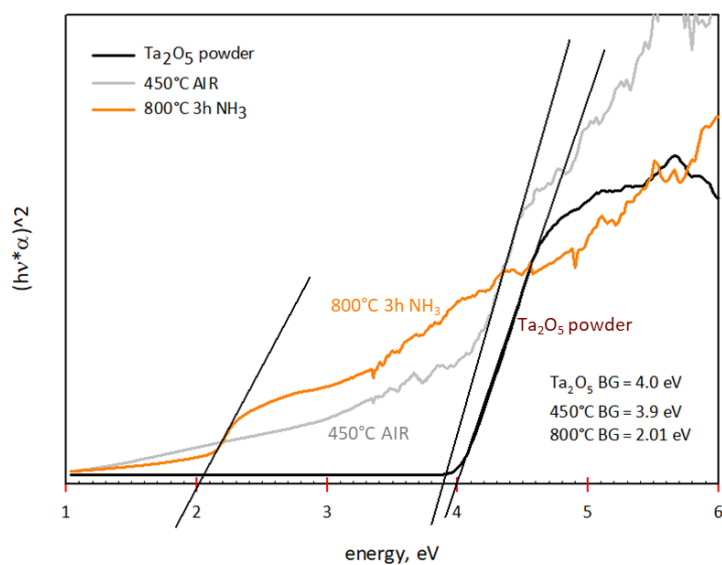


**Figure 9**. Band gap energy (Eg) determination from Tauc plot.

**Photobehavior of the $TaO_xN_x$ NTs film array and structure-activity relations**

***Photocurrent performances.*** Figure 10 shows the results of the photocurrent measurements using an AM 1.5G filter, simulating the standard terrestrial solar distribution. This filter was used for all the tests. Figure 10a shows the photocurrent measurements for the samples prepared at different voltages and nitrided at the same temperature (700°C). The sample anodised at 40 V (see figure 10a) gave the

highest photocurrent response (with respect to the sample prepared at 20 and 60 V). The sample prepared at 40 V has a tube diameter of about 65-70 nm and a tube length of less than 2 µm. Figure 10b shows the differences in the photocurrent between two samples anodised at 40 V but treated with ammonia at different temperatures. The nitridation temperature has a positive effect in terms of photocurrent. This result is related to the higher substitution of N into the $Ta_2O_5$ lattice with No content increasing from 13.5% to 15.0%, see Figure 7.
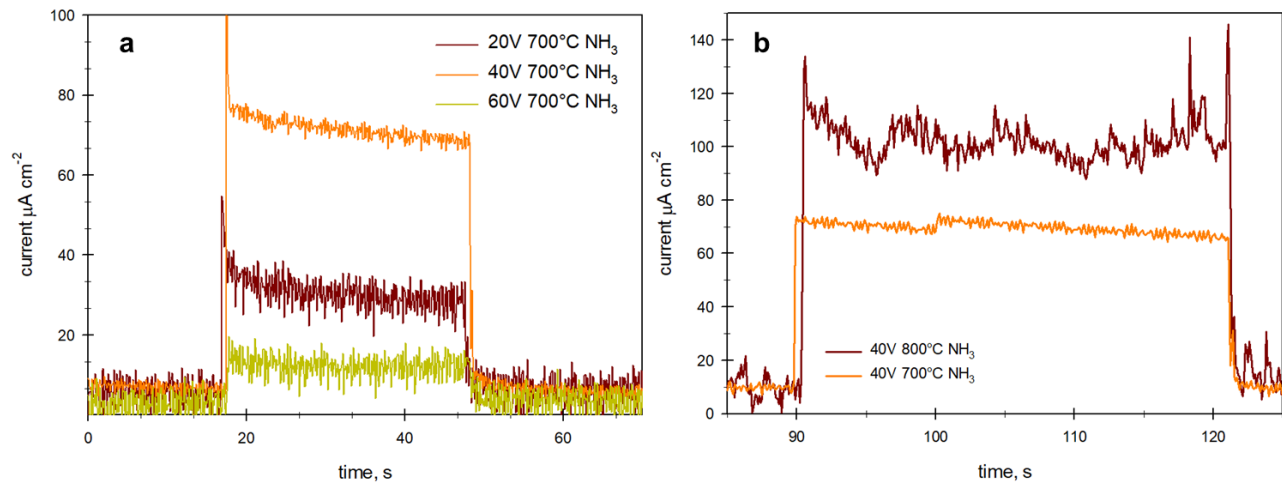


**Figure 10**. a) Photocurrent signals under AM 1.5G illumination of $TaO_xN_x$ NTs film array prepared at different voltages; b) photocurrent signals for 40 V anodised sample with different nitridation temperatures.

***Methylene blue (MB) degradation tests***. MB photodegradation tests were used as model tests to analyze the photo performances of the $TaO_xN_x$ NTs film array. The results are reported in Figure 11a. In contrast, Figure 11b reports the relationship between the MB degradation rate and the atomic percentages wt. of nitrogen (N%) in the NTs film array samples. The $Ta_2O_5$ powder has nearly negligible activity, while the $Ta_2O_5$ NTs film array shows some activity, consistently with a slight shift of the BG to the visible region. The partial substitution of oxygen with nitrogen due to nitridation increases the degradation rate. Still, there is a drastic change above 700°C in agreement with the development a clear band around 500 nm in the UV-visible spectrum (Figure 8) associated with the formation of a more ordered crystalline structure and the thermal annealing of defects. Thus, in addition to the change in the band gap associated with the degree of substitution of oxygen with nitrogen, the presence of defects induced by the treatment negatively influences photocatalytic performances. A temperature above 700°C is thus necessary to reduce these defects and improve photocatalytic performances. However, as commented before, temperatures of treatment with ammonia above 800°C lead to mechanically fragile films which cannot be used for the catalytic tests.
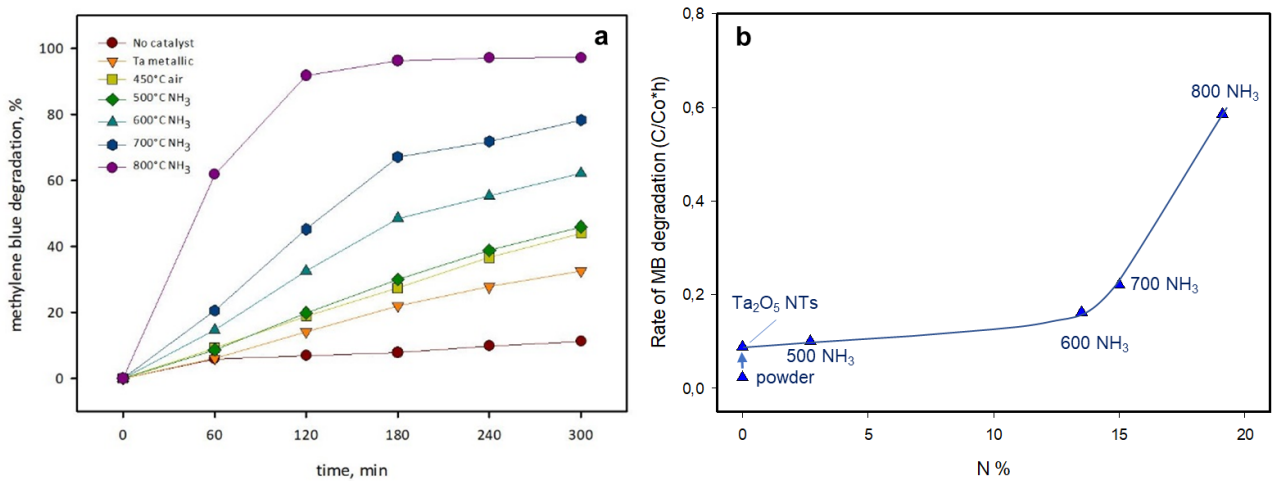
**Figure 11**. a) Methylene blue degradation as a function of time under AM 1.5 G solar simulator filter and using different TaOxNy NTs photocatalysts; b) Relationship between the rate of MB degradation and the atomic percentages wt. of nitrogen (N%) in the NTs film array samples.

***Ethanol photoreforming to produce H₂.*** The photocatalytic behaviour of the materials produced was also tested in the gas phase ethanol photo-reforming to produce $H_2$ [29]. Figure 12 shows the $H_2$ production rate ($\mu mol \cdot min^{-1}$) obtained for $Ta_2O_5$ powder (Sigma Aldrich - SA) before or after annealing in an ammonia flow at 900°C (3 h) and for $Ta_2O_5$ NTs film arrays. The two power samples were spray-coated onto metallic Ta to form a film similar to that of NTs film array. The results show a higher $H_2$ production rate of $Ta_2O_5$ NTs film array than $Ta_2O_5$ powder. This effect is likely associated with the BG shifts due to nanostructure.
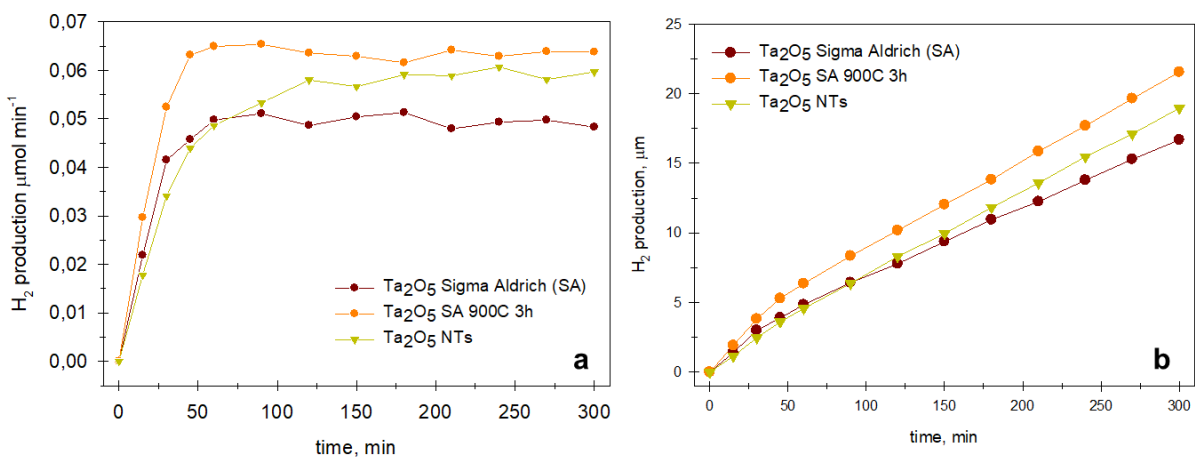


**Figure 12**. a) $H_2$ evolution during ethanol photo-reforming experiments using $Ta_2O_5$ NTs and Sigma Aldrich (SA) $Ta_2O_5$ powder as reference (before and after nitridation at 900°C for 3h), b) cumulative $H_2$ production during 5h tests.

Ta$_2$O$_5$ (SA) treated with ammonia at 900°C instead provided the highest H$_2$ productivity due to the higher absorbance in the visible region. TaO$_x$N$_y$ NTs film array cannot be tested in this reactor due to their scarce robustness. However, when their mechanical resistance could be improved, allowing their use in this type of photoreactors, Figure 12 suggest their practical use as efficient photoanodes for H$_2$ production by ethanol photo-reforming.

***Photo-assisted H$_2$ generation tests***. These were made in an H-type cell at 2V vs Ag/AgCl (see the materials and methods section). Two samples were used for these tests: i) Ta$_2$O$_5$ NTs and TaO$_x$N$_y$ NTs film arrays. Both samples were prepared with the same synthesis parameters (40V/40V), but the oxy-nitride sample was annealed in ammonia at 800°C for 3h. The active surface area is 1cm sq. The results are reported in Figure 13.
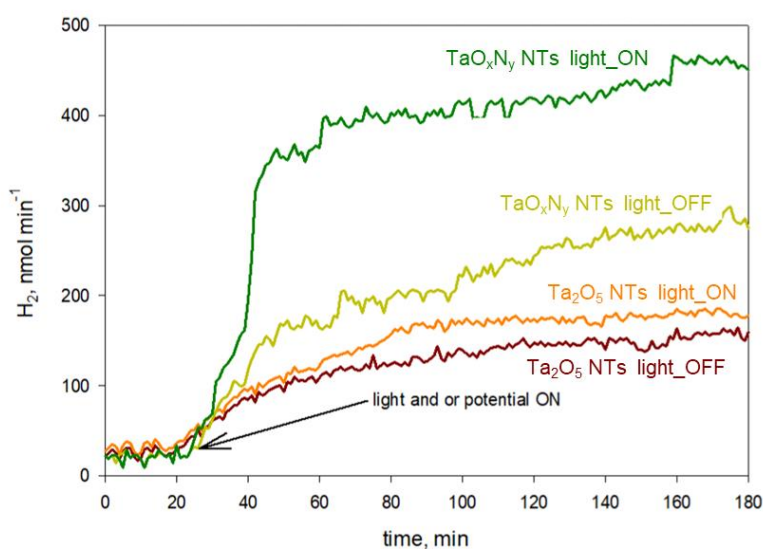


**Figure 13**. The H$_2$ production rate in an H-type cell operating at 2V vs Ag/AgCl for NTs film-array in the oxide and nitride form. At 20 min, the potential is switched on in the presence or not also of light irradiation. Without light, the generation of H2 occurs by electrolysis. With light_on by photo-assisted electrolysis.

In these photo-assisted H$_2$ generation tests, at 20 min, the potential (2V) is switched, monitoring the rate of H$_2$ production by electrolysis, in the absence or presence of light irradiation. The first corresponds thus to the electrolysis case, and the second is the photo-assisted electrolysis case. The results show that Ta oxide possesses a very low activity under AM 1.5 G solar light due to the BG in the UV region. The difference in the H$_2$ production is minor between electrolysis and photo-assisted electrolysis. Differently, the nitride sample shows a large increment in photo-assisted H$_2$ production (about 37%) compared to the electrolysis case. The increment is 62% if we compare the nitride with the oxide sample.

**Conclusions**

This work demonstrates that tantalum oxide NTs arrays can be successfully synthesised through a two-step anodisation process. The choice of the synthesis parameters allowed us to obtain the desired morphology, the nanotube length varying from 2µm up to 5µm, and the inner tube diameter ranging from 20 nm to 100 nm. To improve the absorbance in the visible region, the tantalum oxide samples were successfully converted in $TaO_xN_y$ NTs film array via high-temperature annealing under ammonia flow. The band gap shifts from 4.2 eV of the bare tantalum oxide to 2.1 eV of the sample treated at 800°C. EDX analysis showed that increasing the nitridation temperature increases the amount of nitrogen present in the lattice of the nanotubes going from 2.7% for the sample treated at 500°C to about 19% for the sample prepared at 900°C. Increasing the degree of substitution of N leads to enhanced photocatalytic performances, as shown by chrono-amperometry measurements. The sample prepared at 800°C shows a higher photocurrent value (120 nA·cm$^{-2}$).

Three different types of photoactivity tests were made. MB degradation confirms that the degree of substitution of N increases the catalytic activity of the $TaO_xN_y$ NTs film array. The increase is not linear because, increasing the annealing temperature in the NH$_3$ atmosphere, a reduction in the defectivity also occurs. Above about 700°C, thus, a drastic change in the rate of MD degradation as a function of the increase in nitridation degree occurs. The sample with the higher amount of N (800°C) shows the best degradation rate that reaches almost 100% in just 180 min of irradiation. However, at higher annealing temperatures, the loss in mechanical stability prevents further improvement of the performances.

Ethanol photoreforming tests show that both the presence of a nanostructure and N's degree of substitution positively affect H$_2$ production. Photo-assisted H$_2$ generation tests also show the promotion effect in the visible-light activity by the nanostructure and the formation of an oxy-nitride. The $TaO_xN_y$ NTs film array shows an H$_2$ production 37% higher in the photo-assisted process than only electrolysis and 62% higher than the $Ta_2O_5$ NTs film array electrode.

In conclusion, the $TaO_xN_y$ NTs film array electrodes are good candidates for photo and photoelectrochemical applications. However, the mechanical robustness has to be improved. In particular, the results presented here indicate the interface oxide layer between the NTs and the Ta substrate as the critical element.

## References

## References

[1]    S. Horikoshi, N. Serpone, Can the photocatalyst TiO2 be incorporated into a wastewater treatment method? Background and prospects, Catalysis Today, 340 (2020) 334-346.

[2]    J. You, Y. Guo, R. Guo, X. Liu, A review of visible light-active photocatalysts for water disinfection: Features and prospects, Chemical Engineering Journal, 373 (2019) 624-641.

[3]    W.-H. Chen, J.E. Lee, S.-H. Jang, S.-S. Lam, G.H. Rhee, K.-J. Jeon, M. Hussain, Y.-K. Park, A review on the visible light active modified photocatalysts for water splitting for hydrogen production, International Journal of Energy Research, 46 (2022) 5467-5477.

[4]    R. Kaushik, P.K. Singh, A. Halder, Modulation strategies in titania photocatalyst for energy recovery and environmental remediation, Catalysis Today, 384-386 (2022) 45-69.

[5]    S. Martha, P. Chandra Sahoo, K.M. Parida, An overview on visible light responsive metal oxide based photocatalysts for hydrogen energy production, RSC Advances, 5 (2015) 61535-61553.

[6]    A.B. Djurišić, Y. He, A.M.C. Ng, Visible-light photocatalysts: Prospects and challenges, APL Materials, 8 (2020) 030903.

[7]    G. Centi, S. Perathoner, Catalysis for an Electrified Chemical Production, Catalysis Today, (2022).

[8]    G. Centi, S. Perathoner, Redesign chemical processes to substitute the use of fossil fuels: A viewpoint of the implications on catalysis, Catalysis Today, 387 (2022) 216-223.

[9]    G. Centi, S. Perathoner, Status and gaps toward fossil-free sustainable chemical production, Green Chemistry, 24 (2022) 7305-7331.

[10]   G. Papanikolaou, G. Centi, S. Perathoner, P. Lanzafame, Catalysis for e-Chemistry: Need and Gaps for a Future De-Fossilized Chemical Production, with Focus on the Role of Complex (Direct) Syntheses by Electrocatalysis, ACS Catalysis, 12 (2022) 2861-2876.

[11]   P. Lanzafame, S. Abate, C. Ampelli, C. Genovese, R. Passalacqua, G. Centi, S. Perathoner, Beyond Solar Fuels: Renewable Energy-Driven Chemistry, ChemSusChem, 10 (2017) 4409-4419.

[12]   A. Fujishima, K. Honda, Electrochemical Photolysis of Water at a Semiconductor Electrode, Nature, 238 (1972) 37-38.

[13]   H. Nishiyama, T. Yamada, M. Nakabayashi, Y. Maehara, M. Yamaguchi, Y. Kuromiya, Y. Nagatsuma, H. Tokudome, S. Akiyama, T. Watanabe, R. Narushima, S. Okunaka, N. Shibata, T. Takata, T. Hisatomi, K. Domen, Photocatalytic solar hydrogen production from water on a 100-m2 scale, Nature, 598 (2021) 304-307.

[14] V. Romano, G. D'Angelo, S. Perathoner, G. Centi, Current density in solar fuel technologies, Energy & Environmental Science, 14 (2021) 5760-5787.

[15] C. Ampelli, C. Genovese, B.C. Marepally, G. Papanikolaou, S. Perathoner, G. Centi, Electrocatalytic conversion of CO2 to produce solar fuels in electrolyte or electrolyte-less configurations of PEC cells, Faraday Discussions, 183 (2015) 125-145.

[16] C. Ampelli, C. Genovese, R. Passalacqua, S. Perathoner, G. Centi, A gas-phase reactor powered by solar energy and ethanol for H2 production, Applied Thermal Engineering, 70 (2014) 1270-1275.

[17] C. Ampelli, G. Centi, R. Passalacqua, S. Perathoner, Electrolyte-less design of PEC cells for solar fuels: Prospects and open issues in the development of cells and related catalytic electrodes, Catalysis Today, 259 (2016) 246-258.

[18] S. Perathoner, G. Centi, D. Su, Turning Perspective in Photoelectrocatalytic Cells for Solar Fuels, ChemSusChem, 9 (2016) 345-357.

[19] T. Saboo, F. Tavella, C. Ampelli, S. Perathoner, C. Genovese, B.C. Marepally, L. Veyre, E.A. Quadrelli, G. Centi, Water splitting on 3D-type meso/macro porous structured photoanodes based on Ti mesh, Solar Energy Materials and Solar Cells, 178 (2018) 98-105.

[20] J.F. de Brito, F. Tavella, C. Genovese, C. Ampelli, M.V.B. Zanoni, G. Centi, S. Perathoner, Role of CuO in the modification of the photocatalytic water splitting behavior of TiO2 nanotube thin films, Applied Catalysis B: Environmental, 224 (2018) 136-145.

[21] F. Tavella, C. Ampelli, L. Frusteri, F. Frusteri, S. Perathoner, G. Centi, Development of photoanodes for photoelectrocatalytic solar cells based on copper-based nanoparticles on titania thin films of vertically aligned nanotubes, Catalysis Today, 304 (2018) 190-198.

[22] M. Ge, Q. Li, C. Cao, J. Huang, S. Li, S. Zhang, Z. Chen, K. Zhang, S.S. Al-Deyab, Y. Lai, One-dimensional TiO2 Nanotube Photocatalysts for Solar Water Splitting, Advanced Science, 4 (2017) 1600152.

[23] O.K. Varghese, C.A. Grimes, Appropriate strategies for determining the photoconversion efficiency of water photoelectrolysis cells: A review with examples using titania nanotube array photoanodes, Solar Energy Materials and Solar Cells, 92 (2008) 374-384.

[24] X. Hou, Z. Li, L. Fan, J. Yuan, P.D. Lund, Y. Li, Effect of Ti foil size on the micro sizes of anodic TiO2 nanotube array and photoelectrochemical water splitting performance, Chemical Engineering Journal, 425 (2021) 131415.

[25] K. Arifin, R.M. Yunus, L.J. Minggu, M.B. Kassim, Improvement of TiO2 nanotubes for photoelectrochemical water splitting: Review, International Journal of Hydrogen Energy, 46 (2021) 4998-5024.

[26] R. Passalacqua, S. Perathoner, G. Centi, Semiconductor, molecular and hybrid systems for photoelectrochemical solar fuel production, Journal of Energy Chemistry, 26 (2017) 219-240.

[27] G. Centi, R. Passalacqua, S. Perathoner, Advanced nanostructured titania photoactive materials for sustainable H2 production, Materials Science in Semiconductor Processing, 42 (2016) 115-121.

[28] R. Passalacqua, S. Perathoner, G. Centi, Use of modified anodization procedures to prepare advanced TiO2 nanostructured catalytic electrodes and thin film materials, Catalysis Today, 251 (2015) 121-131.

[29] C. Ampelli, R. Passalacqua, C. Genovese, S. Perathoner, G. Centi, T. Montini, V. Gombac, J.J. Delgado Jaen, P. Fornasiero, H2 production by selective photo-dehydrogenation of ethanol in gas and liquid phase on CuOx/TiO2 nanocomposites, RSC Advances, 3 (2013) 21776-21788.

[30] H. Kisch, W. Macyk, Visible-Light Photocatalysis by Modified Titania, ChemPhysChem, 3 (2002) 399-400.

[31] Y. Yang, H. Zhong, C. Tian, Photocatalytic mechanisms of modified titania under visible light, Research on Chemical Intermediates, 37 (2011) 91-102.

[32] N. Kaur, S.K. Shahi, J.S. Shahi, S. Sandhu, R. Sharma, V. Singh, Comprehensive review and future perspectives of efficient N-doped, Fe-doped and (N,Fe)-co-doped titania as visible light active photocatalysts, Vacuum, 178 (2020) 109429.

[33] V.H. Nguyen, B.H. Nguyen, Visible light responsive titania-based nanostructures for photocatalytic, photovoltaic and photoelectrochemical applications, Advances in Natural Sciences: Nanoscience and Nanotechnology, 3 (2012) 023001.

[34] M. Ahmed, G. Xinxin, A review of metal oxynitrides for photocatalysis, Inorganic Chemistry Frontiers, 3 (2016) 578-590.

[35] T. Takata, C. Pan, K. Domen, Recent progress in oxynitride photocatalysts for visible-light-driven water splitting, Science and Technology of Advanced Materials, 16 (2015) 033506.

[36] M. Sakar, R.M. Prakash, K. Shinde, G.R. Balakrishna, Revisiting the materials and mechanism of metal oxynitrides for photocatalysis, International Journal of Hydrogen Energy, 45 (2020) 7691-7705.

[37] M. Xiao, S. Wang, S. Thaweesak, B. Luo, L. Wang, Tantalum (Oxy)Nitride: Narrow Bandgap Photocatalysts for Solar Hydrogen Generation, Engineering, 3 (2017) 365-378.

[38] D. Cristea, L. Cunha, C. Gabor, I. Ghiuta, C. Croitoru, A. Marin, L. Velicu, A. Besleaga, B. Vasile, Tantalum Oxynitride Thin Films: Assessment of the Photocatalytic Efficiency and Antimicrobial Capacity, Nanomaterials, 2019.

[39]   E. Nurlaela, A. Ziani, K. Takanabe, Tantalum nitride for photocatalytic water splitting: concept and applications, Materials for Renewable and Sustainable Energy, 5 (2016) 18.

[40]   V. Khanal, R. Irani, S. Fiechter, F.F. Abdi, V. Subramanian, Editors' Choice—The Photoelectrochemical and Photocatalytic Properties of Tantalum Oxide and Tantalum Nitride, Journal of The Electrochemical Society, 166 (2019) H3294.

[41]   C. Zhen, R. Chen, L. Wang, G. Liu, H.-M. Cheng, Tantalum (oxy)nitride based photoanodes for solar-driven water oxidation, Journal of Materials Chemistry A, 4 (2016) 2783-2800.

[42]   C. Zhen, L. Wang, G. Liu, G.Q. Lu, H.-M. Cheng, Template-free synthesis of Ta3N5 nanorod arrays for efficient photoelectrochemical water splitting, Chemical Communications, 49 (2013) 3019-3021.

[43]   L. Wang, N.T. Nguyen, X. Zhou, I. Hwang, M.S. Killian, P. Schmuki, Enhanced Charge Transport in Tantalum Nitride Nanotube Photoanodes for Solar Water Splitting, ChemSusChem, 8 (2015) 2615-2620.

[44]   Y. Du, L. Zhao, Y. Chang, Y. Su, Tantalum (oxy)nitrides nanotube arrays for the degradation of atrazine in vis-Fenton-like process, Journal of Hazardous Materials, 225-226 (2012) 21-27.

[45]   J.E. Barton, C.L. Stender, P. Li, T.W. Odom, Structural control of anodized tantalum oxide nanotubes, Journal of Materials Chemistry, 19 (2009) 4896-4898.

[46]   Z. Su, S. Grigorescu, L. Wang, K. Lee, P. Schmuki, Fast fabrication of Ta2O5 nanotube arrays and their conversion to Ta3N5 for efficient solar driven water splitting, Electrochemistry Communications, 50 (2015) 15-19.

[47]   R.V. Gonçalves, P. Migowski, H. Wender, D. Eberhardt, D.E. Weibel, F.C. Sonaglio, M.J.M. Zapata, J. Dupont, A.F. Feil, S.R. Teixeira, Ta2O5 Nanotubes Obtained by Anodization: Effect of Thermal Treatment on the Photocatalytic Activity for Hydrogen Production, The Journal of Physical Chemistry C, 116 (2012) 14022-14030.

[48]   I.V. Sieber, P. Schmuki, Porous Tantalum Oxide Prepared by Electrochemical Anodic Oxidation, Journal of The Electrochemical Society, 152 (2005) C639.

[49]   V. Khanal, E. Soto-Harrison, D. Chandra, N.O. Balayeva, D.W. Bahnemann, V. Subramanian, A Selective Synthesis of TaON Nanoparticles and Their Comparative Study of Photoelectrochemical Properties,  Catalysts, 2020.

[50]   M.A. Baluk, M.P. Kobylański, W. Lisowski, G. Trykowski, T. Klimczuk, P. Mazierski, A. Zaleska-Medynska, Fabrication of Durable Ordered Ta2O5 Nanotube Arrays Decorated with Bi2S3 Quantum Dots,  Nanomaterials, 2019.

[51]   F. Riboni, N.T. Nguyen, S. So, P. Schmuki, Aligned metal oxide nanotube arrays: key-aspects of anodic TiO2 nanotube formation and properties, Nanoscale Horizons, 1 (2016) 445-466.

[52] B.E. Sanabria Arenas, A. Strini, L. Schiavi, A. Li Bassi, V. Russo, B. Del Curto, M.V. Diamanti, M. Pedeferri, Photocatalytic Activity of Nanotubular TiO2 Films Obtained by Anodic Oxidation: A Comparison in Gas and Liquid Phase,  Materials, 2018.

[53] X. Nie, S. Yin, W. Duan, Z. Zhao, L. Li, Z. Zhang, Recent Progress in Anodic Oxidation of TiO2 Nanotubes and Enhanced Photocatalytic Performance: A Short Review, Nano, 16 (2021) 2130002.

[54] C. Ampelli, F. Tavella, S. Perathoner, G. Centi, Engineering of photoanodes based on ordered TiO2-nanotube arrays in solar photo-electrocatalytic (PECa) cells, Chemical Engineering Journal, 320 (2017) 352-362.

[55] C. Ampelli, F. Tavella, C. Genovese, S. Perathoner, M. Favaro, G. Centi, Analysis of the factors controlling performances of Au-modified TiO2 nanotube array based photoanode in photo-electrocatalytic (PECa) cells, Journal of Energy Chemistry, 26 (2017) 284-294.

[56] C. Ampelli, C. Genovese, G. Centi, R. Passalacqua, S. Perathoner, Nanoscale Engineering in the Development of Photoelectrocatalytic Cells for Producing Solar Fuels, Topics in Catalysis, 59 (2016) 757-771.

[57] X. Feng, T.J. LaTempa, J.I. Basham, G.K. Mor, O.K. Varghese, C.A. Grimes, Ta3N5 Nanotube Arrays for Visible Light Water Photoelectrolysis, Nano Letters, 10 (2010) 948-952.

[58] P. Makuła, M. Pacia, W. Macyk, How To Correctly Determine the Band Gap Energy of Modified Semiconductor Photocatalysts Based on UV–Vis Spectra, The Journal of Physical Chemistry Letters, 9 (2018) 6814-6817.